

Nanosecond Structural Dynamics during Electrical Melting of Charge Density Waves in 1T-TaS₂

Daniel B. Durham¹, Thomas E. Gage², Connor P. Horn^{1,3}, Xuedan Ma,²

Haihua Liu,² Ilke Arslan,² Supratik Guha,^{1,3} and Charudatta Phatak^{1,4,*}

¹Materials Science Division, Argonne National Laboratory, Lemont, Illinois 60439, USA

²Center for Nanoscale Materials, Argonne National Laboratory, Lemont, Illinois 60439, USA

³Pritzker School of Molecular Engineering, University of Chicago, Chicago, Illinois 60637, USA

⁴Department of Materials Science and Engineering, Northwestern University, Evanston, Illinois, 60208, USA



(Received 14 June 2023; revised 27 November 2023; accepted 25 April 2024; published 28 May 2024)

Electrical control of charge density waves has been of immense interest, as the strong underlying electron-lattice interactions potentially open new, efficient pathways for manipulating their ordering and, consequently, their electronic properties. However, the transition mechanisms are often unclear as electric field, current, carrier injection, heat, and strain can all contribute and play varying roles across length scales and timescales. Here, we provide insight on how electrical stimulation melts the room temperature charge density wave order in 1T-TaS₂ by visualizing the atomic and mesoscopic structural dynamics from quasi-static to nanosecond pulsed melting. Using a newly developed ultrafast electron microscope setup with electrical stimulation, we reveal the order and strain dynamics during voltage pulses as short as 20 ns. The order parameter dynamics across a range of pulse amplitudes and durations support a thermally driven mechanism even for fields as high as 19 kV cm⁻¹. In addition, time-resolved imaging reveals a heterogeneous, mesoscopic strain response across the flake, including MHz-scale acoustic resonances that emerge during sufficiently short pulsed excitation which may modulate the order. These results suggest that metallic charge density wave phases like studied here may be more robust to electronic switching pathways than insulating ones, motivating further investigations at higher fields and currents in this and other related systems.

DOI: [10.1103/PhysRevLett.132.226201](https://doi.org/10.1103/PhysRevLett.132.226201)

In strongly correlated materials, electron-electron and electron-lattice interactions lead to a rich landscape of ordered structural phases [1–4]. This coupling can also make order in these systems more sensitive to electronic excitations, opening unconventional routes to control electronic properties [3]. Charge density waves (CDWs) have proven especially interesting in this respect: Both optical and electrical excitation have been shown to rapidly drive many types of CDWs into new states, often mediating insulator-metal transitions [5,6] and in some cases forming transient or metastable nonequilibrium phases [5,7–10]. Among these, electrical stimulation provides unique transition pathways via electric fields, currents, and injected carriers [7,11]. However, it is often unclear whether electrically stimulated CDW transitions are driven by electrical factors or secondary effects such as heat or strain. Disentangling the contributing factors across varying timescales and length scales is crucial to understand the true mechanisms of electrical CDW manipulation.

In this context, 1T-TaS₂ is a valuable system to study. First, it can be stabilized in one of a few distinct CDW states by controlling the temperature, including the insulating commensurate (CCDW) state at low temperatures, consisting of fully interlocked 13-atom hexagram-shaped

clusters [12]; the conductive nearly commensurate (NCCDW) phase at room temperature, with hexagonal domains of interlocked clusters separated by discommensurate boundaries [12,13]; the even more conducting incommensurate (ICCDW) phase above ≈ 350 K [12,14], and the normal metallic (*M*) phase above ≈ 550 K [15]. Second, both optical and electrical stimulation have been shown to induce a variety of rapid CDW transformations. Pulsed lasers can induce switching from CCDW and NCCDW to various other states on subpicosecond timescales [5,16], including forming a metastable conducting “hidden” state from CCDW [17]. Electrically, the CCDW state can also be switched to the other high temperature CDW states [6,18] or a hidden state [7,19,20], attributed to carrier injection driving band gap collapse.

Unlike CCDW, the room-temperature NCCDW represents a CDW which introduces a gap below the Fermi level [14] and hence remains metallic, albeit with 2–3 times higher resistivity than ICCDW or *M* [14,15,18]. Electrical stimulation appears to induce switching to the ICCDW or even the *M* phase [18], leading to proof-of-concept devices leveraging these transitions such as high-frequency oscillators for neuromorphic computing [21,22]. However, the transition mechanism is not fully understood, having been

ascribed to carrier injection [23], field-driven depinning [24], self-heating [18,25], or a combination thereof [24,26]. So far, this has mainly been investigated via electrical measurements in combination with Joule heating simulations. The structural dynamics, especially during pulsed excitation, have not yet been reported.

Here, we address this by employing a new ultrafast transmission electron microscopy (UEM) capability at the Center for Nanoscale Materials at Argonne National Laboratory [27] with electrical pulse stimulation. Using this, we reveal the atomic and mesoscopic structural dynamics during electrical melting of the NCCDW at room temperature in a suspended TaS₂ flake down to 20 ns pulses with subnanosecond temporal resolution. The order parameter dynamics support the robustness of the NCCDW to field or current-driven mechanisms even in nanosecond-scale pulses. Meanwhile, the mesoscopic strain dynamics reveal emergent acoustic resonances in short pulsed excitation which appear to dynamically modulate the CDW order.

First, an electrically contacted freestanding TaS₂ flake specimen suitable for *in situ* transmission electron microscopy (TEM) was prepared as shown in Fig. 1(a). The specimen chips provided by DENSsolutions included gold electrodes (180 nm thick) routed to a 5 μm through-hole patterned on a suspended, 450 nm thick silicon nitride membrane. They also feature a surrounding resistive heating spiral (inner radius about 70 μm) to independently control the specimen temperature. Focused Ga ion beam milling was used to create a narrower, 1 μm wide through-hole (13.5 μm in length) with 1 μm wide, 100 nm thick Pt electrodes deposited on either side using ion beam-induced deposition (IBID). A 100 nm thick flake of TaS₂ was then exfoliated and dry transferred across these electrodes using polydimethylsiloxane (PDMS) stamps [28].

TEM visualizes the initial structural state of the flake. Bright-field imaging [Fig. 1(b)] shows that the TaS₂ flake fully spans the gap. In addition, dark bands indicate regions of common tilt orientation that meet a strong diffraction condition, outlining “bend contours” [29] which visualize rippling in the freestanding gap. An electron beam shower in the microscope was used to stabilize the electrical contact. A selected area electron diffraction (SAED) pattern recorded where the electrodes first reach the gap [Fig. 1(c)] shows that the crystal flake is oriented close to the [001] zone axis. Six second-order superlattice peaks surround each primary lattice peak, indicative of the NCCDW state where the modulation vectors are rotated $\approx 12^\circ$ from the primary lattice (first-order satellites are not strongly excited at [001] due to stacking periodicity) [13,30]. We then characterized the steady-state phase transformations in this device using simultaneous SAED and two-wire resistance measurement during temperature and bias sweeps (8.1 K/min and 40 mV/min, respectively), shown in Fig. 1(e). The NCCDW signal is calculated from SAED

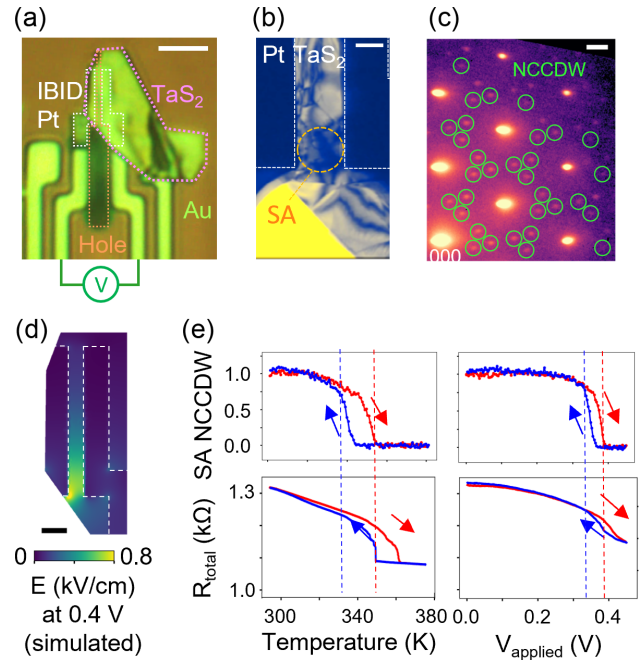


FIG. 1. Freestanding TaS₂ lateral device for *in situ* and ultrafast electrical stimulation in TEM. (a) Optical microscope image of the TaS₂ flake exfoliated on the TEM-compatible chip with electrodes. IBID Pt is by ion beam induced deposition. Scale = 10 μm . (b) Bright-field TEM image. Scale = 1 μm . (c) Selected area electron diffraction (SAED) from circled region in BF TEM image (labeled “SA”). Nearly commensurate charge density wave (NCCDW) superlattice peaks circled in green are used to track the order parameter. Scale = 1 nm^{-1} . (d) Simulated electric field distribution in the TaS₂ flake at 0.4 V. Scale = 2 μm . (e) Steady-state thermal and electrical switching characteristics. Integrated signal from NCCDW peaks in selected area (SA NCCDW) drops with the beginning of the total two-wire device resistance (R_{total}) change, showing this region is among the first to melt.

patterns by integrating the superlattice peaks surrounding each primary lattice peak for which all 6 neighboring superlattice peaks are captured on the detector [circled in green in Fig. 1(c), pattern is cropped to one quadrant for ease of viewing]. In both cases, the NCCDW signal disappears at the beginning of a resistance drop. When heating, the resistance transition (monitored using a constant 10 mV bias) is measured to occur between 345 and 360 K, while on cooling it is restored between 350 and 335 K, similar to other works [15,18,24]. The measured resistance change is smaller than observed in some other TaS₂ devices [18], which we attribute to series resistance primarily from the setup and the IBID Pt electrodes. The bias-driven transition starts at around 0.39 V and appears to continue above 0.45 V, but we stopped there to avoid prematurely damaging the specimen. The resistance change occurs over a broader range of temperature and voltage than the NCCDW melting in the selected region, indicating heterogeneous transformation along the gap. We have

directly confirmed this by performing dark-field imaging using a set of three superlattice spots, which shows that the phase transition starts from the maximum field region and progresses along the gap with increasing voltage [31].

To estimate the applied field and resulting temperature rise in the sample during electrical excitation, we performed 3D electromagnetic heating simulations which account for resistive losses and the device geometry (see Supplemental Material [31] and Refs. [18,32–39] therein). The resulting electric field distribution [Fig. 1(d)] is largely concentrated within the gap, providing an estimated 0.7 kV cm^{-1} in the selected region for SAED at the melting threshold of 0.4 V . In addition, the sample temperature is predicted to exceed 350 K —sufficient to thermally melt the NCCDW in these steady state measurements [31].

Compared to static biasing, short electrical pulses can outrun thermal diffusion and access much larger electric fields. To investigate electrical melting dynamics of the NCCDW during nanosecond-scale voltage pulses, we switched to the stroboscopic mode of the UEM. A timing diagram for these measurements is shown in Fig. 2(a). An ultraviolet pulsed laser with 420 ps duration is triggered to generate the sub-ns photoelectron probe pulses. Meanwhile, a second delay generator is triggered to generate synchronized electrical pump pulses with controllable

pump-probe delay, Δt . All stroboscopic measurements in this work were performed at 10 kHz repetition rate. More details about the setup are available in Ref. [41].

We first performed time-resolved electron diffraction, which allows us to simultaneously track the local applied field (via the e-beam deflection) and NCCDW order. We applied 20 ns long pulses at three selected amplitudes and recorded SAED patterns for pump-probe delays ranging from -50 to 300 ns . The time-dependent NCCDW signal for all pulse amplitudes and the e-beam deflection for 11.0 V are shown together in Fig. 2(b).

The measured deflection (θ_{defl}) profile, and hence local applied field, is consistent with the input voltage pulse shape measured separately by an oscilloscope. Also, the deflection magnitude is consistent with that predicted by our electromagnetic simulation. [31] Using

$$\theta_{\text{defl}} = \frac{\lambda}{2\pi} \sigma \int E(z) dz, \quad (1)$$

where σ is the relativistic interaction parameter [42], λ is the de Broglie wavelength, and $E(z)$ is the electric field along the beam path, we calculate an expected $4.6 \mu\text{rad V}^{-1}$, which is close to the measured $3.8 \mu\text{rad V}^{-1}$. This lends confidence to estimating the applied field in the probed region using our simulated electric field distribution: For 11.0 V pulses, the peak field is about 19 kV cm^{-1} .

8.1 V pulses mainly induce a temporary heating without melting the NCCDW: the slight transient reduction in signal is within the range observed in the quasistatic temperature and bias sweeps before melting [see Fig. 1(e)]. On the other hand, 11.0 and 11.8 V lead to increasing suppression of the NCCDW signal. At these pulse amplitudes, the NCCDW is gradually melted over the duration of the pulse, and shows little change after the pulse ends, slowly recovering before the next pulse arrives $100 \mu\text{s}$ later. Had the NCCDW signal immediately recovered after the field was removed, this would be strong evidence for a transient field or current-driven melting that reforms upon thermalization. Or, if it had shown immediate transition at the pulse edges, this would indicate transformation via carrier injection during temporal field gradients like proposed for electrical formation of hidden states in the CCDW [7]. Instead, the transformation is gradual and is at least metastable if not thermally stabilized. In addition, we find the NCCDW signal shows strong correspondence to the time-dependent accumulated pulse energy across the three pulse amplitudes, indicating a thermally driven transition [31].

We then investigated the dependence of switching dynamics on pulse duration, which provides further evidence for a thermally driven transition. The NCCDW signal at a fixed delay time of 340 ns as a function of pulse amplitude and duration is shown in Fig. 3. Here, it is evident that the electric field amplitude required to drive the

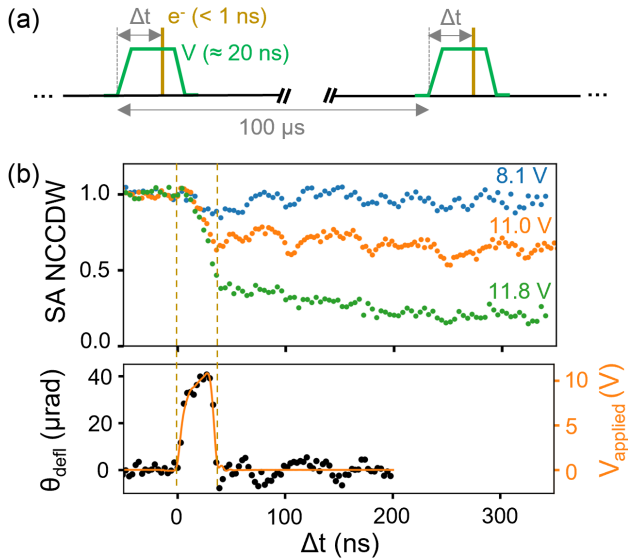


FIG. 2. Electrical melting dynamics of the NCCDW order during 20 ns voltage pulses tracked by nanosecond electron diffraction. (a) Timing diagram for stroboscopic ultrafast electron microscopy measurements. Synchronized voltage “pump” and electron “probe” pulses separated by a variable pump-probe delay Δt are delivered at 10 kHz repetition rate. (b) Time-resolved NCCDW signal in the selected area (SA NCCDW) for varying pulse amplitudes (top) and electron probe deflection, which tracks the local applied field, for 11.0 V pulse amplitude (bottom, black dots). Yellow dashed vertical lines indicate start and end of the voltage pulse. The input voltage pulse shape measured by an oscilloscope is superimposed (bottom, orange line).

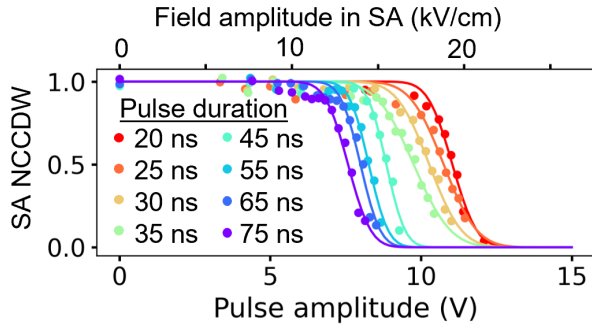


FIG. 3. Dependence of the NCCDW melting threshold on pulse duration. The NCCDW signal in the selected area (SA NCCDW) is shown as a function of pulse amplitude for varying pulse durations, probed at $\Delta t = 340$ ns. Solid lines are error function fits. The conversion factor to generate the upper electric field axis from the voltage is calculated using electromagnetic simulation of the device [31].

transition continually increases as pulse duration decreases from 75 to 20 ns, and is more than 25 times larger than that required at steady state. This suggests that over this range, the melting is not field or current driven as suggested for certain pulsed CCDW transitions which showed a duration- and temperature-independent current threshold [7]. We have also performed a pulsed Joule heating simulation which supports the plausibility of thermal melting [31]. We note that the required pulse energy appears to increase with duration, likely due to local thermal redistribution on 10's to 100's of ns timescales [31]. We also note that different mechanisms may emerge at lower temperatures and shorter, higher field pulses, especially in the CCDW state.

In addition to raising the temperature, electrical stimulation can also generate strain, allowing us to study the effects of dynamic strain on the CDW order. On one hand, thermally generated strain should have a small contribution to NCCDW melting compared to the heating itself: the thermal expansion mismatch-induced lateral pressure should be less than 20 MPa [43], whereas hydrostatic pressure-dependent experiments find ≈ 2.5 GPa is required to dissolve the NCCDW state at 300 K [15,44]. On the other, short pulsed excitation can launch coherent phonons which could impart stronger effects. To visualize the strain dynamics across the flake during pulsed excitation, we performed stroboscopic bright-field TEM imaging. Pump-probe delay was varied from -50 to 420 ns and back, and the two sweeps were averaged.

The change in BF signal relative to the image at $\Delta t = 0$ ns during 11.0 V, 20 ns pulses is shown in Fig. 4(a), extracted from the time-resolved movie [31]. The left panel shows the initial BF image with the analysis region highlighted. The right panel shows the time-resolved change of the BF signal in that region as a function of position along the length of the gap. This is expressed as the mean absolute difference ($|\Delta(\text{BF})|$), averaged across the gap. A few behaviors are revealed. Initially, the flake

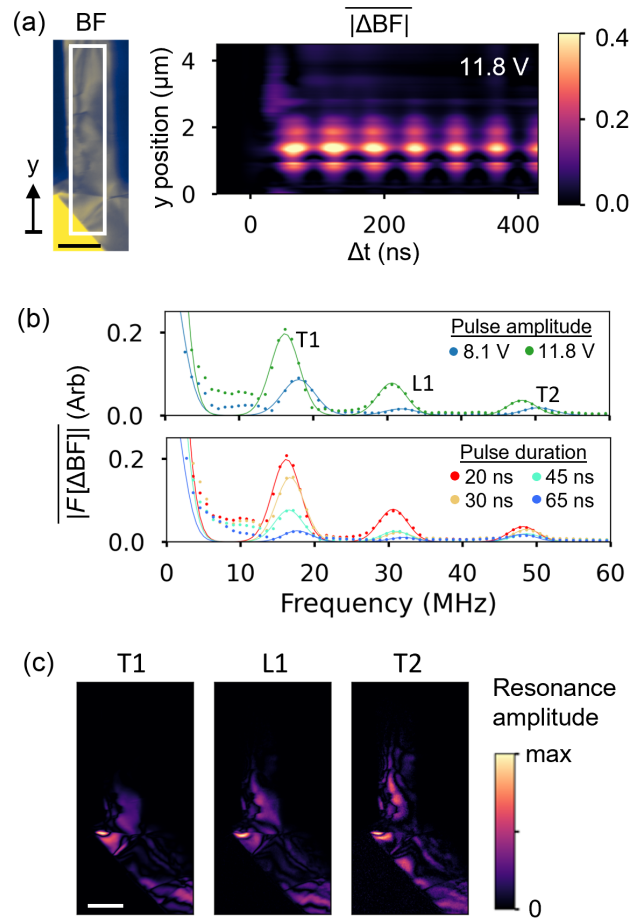


FIG. 4. Mesoscopic strain dynamics revealed by nanosecond electron imaging. (a) (Left) Initial real-space bright-field (BF) TEM image. Region for mean absolute difference analysis is indicated by the white box. Scale = 1 μm . (Right) Time-resolved mean absolute difference of the BF signal ($|\Delta(\text{BF})|$) for varying (y) position along the channel. The mean is computed along the x direction. (b) Fourier transform magnitude of $|\Delta(\text{BF})|$, averaged over the region indicated in panel (a), for varying pulse amplitude and duration. Three acoustic resonance modes are identified, assigned to transverse (T1) and longitudinal (L1) across the length of the flake, and transverse across the width (T2). (c) Resonance signal amplitudes mapped across the flake. Scale = 1 μm .

buckles to accommodate the strain due to heat generation and structural transformation within the pulse duration. This is followed by thermal redistribution as well as prominent bending oscillations due to acoustic resonance.

The frequency content for selected pulse amplitudes and durations is plotted in Fig. 4(b). Three resonance peaks are observed, with larger magnitude for higher amplitude and shorter duration pulses. Using 8.1 V pulses, the resonance frequencies are 18.0, 31.8, and 50.4 MHz. They appear to not be harmonics and can instead be attributed to three separate resonance modes. We assign 18.0 and 31.8 MHz to in-plane transverse (T1) and longitudinal (L1) wave resonances across the 30 μm length of the TaS₂ flake with

velocities of 1.2 and 2.1 km/s, respectively. These are comparable to the in-plane velocities previously reported in bulk 1T-TaS₂ crystals via neutron scattering (1.66 and 2.93 km/s) with the longitudinal and transverse ratio of 1.77 in excellent agreement [45]. We then assign 50.4 MHz to the transverse wave resonance across the 11 μm flake width (T2).

The resonance peaks are present both with and without NCCDW melting, suggesting these are mainly stimulated by thermal shock, though they could be enhanced by the phase transition. There is a small shift in the resonance frequencies with stronger excitation ($\approx 5\%$ lower from 8.1 to 11.8 V), which may be caused by reduced elastic constants, and hence sound velocity, with increasing temperature [46]. Notably, these resonances are only excited when using sufficiently short pulses: For 65 ns or longer pulses, they effectively disappear. Acoustic resonance also manifests as oscillations in the primary lattice peak signals during time-resolved diffraction, and they follow similar amplitude and duration-dependent trends [31]. The amplitude maps for each of the resonance modes [Fig. 4(c)] show that the buckling is largest in the lower region. This is in part because the nearby free edge has more freedom to bend, and also because that is the maximally excited region where most of the acoustic waves are initiated. Additionally, T2 appears to have a different spatial distribution than T1 and L1 arising from the different propagation directions.

Remarkably, there appears to be nearly 10% periodic modulation of the average superlattice peak signal near the T1 resonance frequency for 11.0 V, 20 ns pulses shown in Fig. 2(b). Although diffraction intensities are expected to change with bending as the diffraction condition changes, we find that the comprising superlattice peak intensities all change in the same direction, in contrast to the primary lattice peak changes which show opposite sign across the bending axis. This suggests a genuine modulation of the order parameter (see Supplemental Material [31] and Ref. [40] therein). There has been both theoretical and experimental evidence that static strain modifies the CDW order parameter and the CDW transition temperatures [15,43,44,47]. We propose that when excited near the transition threshold, the oscillating strain caused by acoustic resonance drives dynamic NCCDW melting and reforming at phase boundaries and regions of high local strain. This process would have nanoscale heterogeneity, which is supported by the variation in fluctuation amplitudes found among the individual superlattice peaks despite sampling from a selected area with submicrometer radius [31].

Taken together, these measurements provide strong evidence that electrical melting of the metallic room-temperature NCCDW in 1T-TaS₂ is typically thermally driven, even by nanosecond-scale pulses. That said, there are still opportunities to explore electronically driven

switching mechanisms at lower temperatures, including in the insulating CCDW state [7,19,20], as well as at more extreme length and timescales such as in few or single-layer flakes [23] and by using picosecond current pulses [48]. The measurements also reveal acoustic modes generated during pulsed excitation. On one hand, these could be sources of electrical noise and device failure, though over the course of our measurements we applied billions of pulses without significant damage. On the other hand, they could provide a route to dynamically modulate the CDW and generate high-frequency electronic signals. Furthermore, this work showcases a new capability for UEM to visualize electrically driven dynamics across length and timescales which could be applied to a broad range of electronic materials and devices. For CDWs, further studies of the structural dynamics during pulsed electrical switching in various systems will improve our understanding of the mechanisms for control, the speed limits, and whether nonequilibrium states can be accessed with new properties.

This material is based upon work supported by the U.S. Department of Energy, Office of Science, for support of microelectronics research, under Contract No. DE-AC0206CH11357. Work performed at the Center for Nanoscale Materials, a U.S. Department of Energy Office of Science User Facility, was supported by the U.S. DOE, Office of Basic Energy Sciences, under Contract No. DE-AC02-06CH11357. We acknowledge Yue Li at Argonne National Laboratory for assistance with transferring the TaS₂ flake as well as Yue Cao for valuable discussion.

D. B. D. and T. E. G. contributed equally to this work.

*cd@anl.gov

- [1] M. Imada, A. Fujimori, and Y. Tokura, Metal-insulator transitions, *Rev. Mod. Phys.* **70**, 1039 (1998).
- [2] B. Keimer, S. A. Kivelson, M. R. Norman, S. Uchida, and J. Zaanen, From quantum matter to high-temperature superconductivity in copper oxides, *Nature (London)* **518**, 179 (2015).
- [3] Y. Tokura, M. Kawasaki, and N. Nagaosa, Emergent functions of quantum materials, *Nat. Phys.* **13**, 1056 (2017).
- [4] D. Basov, R. Averitt, and D. Hsieh, Towards properties on demand in quantum materials, *Nat. Phys.* **16**, 1077 (2017).
- [5] T.-R. T. Han, F. Zhou, C. D. Malliakas, P. M. Duxbury, S. D. Mahanti, M. G. Kanatzidis, and C.-Y. Ruan, Exploration of metastability and hidden phases in correlated electron crystals visualized by femtosecond optical doping and electron crystallography, *Sci. Adv.* **1**, e1400173 (2015).
- [6] M. J. Hollander, Y. Liu, W.-J. Lu, L.-J. Li, Y.-P. Sun, J. A. Robinson, and S. Datta, Electrically driven reversible insulator–metal phase transition in 1T-TaS₂, *Nano Lett.* **15**, 1861 (2015).

- [7] I. Vaskivskiy, I. Mihailovic, S. Brazovskii, J. Gospodaric, T. Mertelj, D. Svetin, P. Sutar, and D. Mihailovic, Fast electronic resistance switching involving hidden charge density wave states, *Nat. Commun.* **7**, 11442 (2016).
- [8] X. Shi, W. You, Y. Zhang, Z. Tao, P. M. Oppeneer, X. Wu, R. Thomale, K. Rossnagel, M. Bauer, H. Kapteyn, and M. Murnane, Ultrafast electron calorimetry uncovers a new long-lived metastable state in 1T-TaSe₂ mediated by mode-selective electron-phonon coupling, *Sci. Adv.* **5**, eaav4449 (2019).
- [9] A. Kogar, A. Zong, P. E. Dolgirev, X. Shen, J. Straquadine, Y.-Q. Bie, X. Wang, T. Rohwer, I.-C. Tung, Y. Yang, R. Li, J. Yang, S. Weathersby, S. Park, M. E. Kozina, E. J. Sie, H. Wen, P. Jarillo-Herrero, I. R. Fisher, X. Wang, and N. Gedik, Light-induced charge density wave in LaTe₃, *Nat. Phys.* **16**, 159 (2020).
- [10] K. M. Siddiqui, D. B. Durham, F. Cropp, C. Ophus, S. Rajpurohit, Y. Zhu, J. D. Carlström, C. Stavarakas, Z. Mao, A. Raja, P. Musumeci, L. Z. Tan, A. M. Minor, D. Filippetto, and R. A. Kaindl, Ultrafast optical melting of trimer superstructure in layered 1T'-TaTe₂, *Commun. Phys.* **4**, 152 (2021).
- [11] G. Grüner, The dynamics of charge-density waves, *Rev. Mod. Phys.* **60**, 1129 (1988).
- [12] C. Scruby, P. Williams, and G. Parry, The role of charge density waves in structural transformations of 1T TaS₂, *Philos. Mag.* **31**, 255 (1975).
- [13] A. Spijkerman, J. L. de Boer, A. Meetsma, G. A. Wiegers, and S. van Smaalen, X-ray crystal-structure refinement of the nearly commensurate phase of 1T-TaS₂ in (3 + 2)-dimensional superspace, *Phys. Rev. B* **56**, 13757 (1997).
- [14] Y. Wang, W. Yao, Z. Xin, T. Han, Z. Wang, L. Chen, C. Cai, Y. Li, and Y. Zhang, Band insulator to Mott insulator transition in 1T-TaS₂, *Nat. Commun.* **11**, 4215 (2020).
- [15] B. Sipos, A. F. Kusmartseva, A. Akrap, H. Berger, L. Forró, and E. Tutiš, From Mott state to superconductivity in 1T-TaS₂, *Nat. Phys.* **7**, 960 (2008).
- [16] M. Eichberger, H. Schäfer, M. Krumova, M. Beyer, J. Demsar, H. Berger, G. Moriena, G. Sciaini, and R. D. Miller, Snapshots of cooperative atomic motions in the optical suppression of charge density waves, *Nature (London)* **468**, 799 (2010).
- [17] L. Stojchevska, I. Vaskivskiy, T. Mertelj, P. Kusar, D. Svetin, S. Brazovskii, and D. Mihailovic, Ultrafast switching to a stable hidden quantum state in an electronic crystal, *Science* **344**, 177 (2014).
- [18] A. K. Geremew, S. Rumyantsev, F. Kargar, B. Debnath, A. Nosek, M. A. Bloodgood, M. Bockrath, T. T. Salguero, R. K. Lake, and A. A. Balandin, Bias-voltage driven switching of the charge-density-wave and normal metallic phases in 1T-TaS₂ thin-film devices, *ACS Nano* **13**, 7231 (2019).
- [19] L. Ma, C. Ye, Y. Yu, X. F. Lu, X. Niu, S. Kim, D. Feng, D. Tománek, Y.-W. Son, X. H. Chen, and Y. Zhang, A metallic mosaic phase and the origin of Mott-insulating state in 1T-TaS₂, *Nat. Commun.* **7**, 10956 (2016).
- [20] D. Cho, S. Cheon, K.-S. Kim, S.-H. Lee, Y.-H. Cho, S.-W. Cheong, and H. W. Yeom, Nanoscale manipulation of the Mott insulating state coupled to charge order in 1T-TaS₂, *Nat. Commun.* **7**, 10453 (2016).
- [21] G. Liu, B. Debnath, T. R. Pope, T. T. Salguero, R. K. Lake, and A. A. Balandin, A charge-density-wave oscillator based on an integrated tantalum disulfide–boron nitride–graphene device operating at room temperature, *Nat. Nanotechnol.* **11**, 845 (2016).
- [22] H. Liu, T. Wu, X. Yan, J. Wu, N. Wang, Z. Du, H. Yang, B. Chen, Z. Zhang, F. Liu, W. Wu, J. Guo, and H. Wang, A tantalum disulfide charge-density-wave stochastic artificial neuron for emulating neural statistical properties, *Nano Lett.* **21**, 3465 (2021).
- [23] W. Wen, Y. Zhu, C. Dang, W. Chen, and L. Xie, Raman spectroscopic and dynamic electrical investigation of multi-state charge-wave-density phase transitions in 1T-TaS₂, *Nano Lett.* **19**, 1805 (2019).
- [24] M. Yoshida, Y. Zhang, J. Ye, R. Suzuki, Y. Imai, S. Kimura, A. Fujiwara, and Y. Iwasa, Controlling charge-density-wave states in nano-thick crystals of 1T-TaS₂, *Sci. Rep.* **4**, 7302 (2014).
- [25] A. Mohammadzadeh, S. Baraghani, S. Yin, F. Kargar, J. P. Bird, and A. A. Balandin, Evidence for a thermally driven charge-density-wave transition in 1T-TaS₂ thin-film devices: Prospects for GHz switching speed, *Appl. Phys. Lett.* **118**, 093102 (2021).
- [26] C. Zhu, Y. Chen, F. Liu, S. Zheng, X. Li, A. Chaturvedi, J. Zhou, Q. Fu, Y. He, Q. Zeng, H. J. Fan, H. Zhang, W.-J. Liu, T. Yu, and Z. Liu, Light-tunable 1T-TaS₂ charge-density-wave oscillators, *ACS Nano* **12**, 11203 (2018).
- [27] H. Liu, T. E. Gage, P. Singh, A. Jaiswal, R. D. Schaller, J. Tang, S. T. Park, S. K. Gray, and I. Arslan, Visualization of plasmonic couplings using ultrafast electron microscopy, *Nano Lett.* **21**, 5842 (2021).
- [28] A. Castellanos-Gomez, M. Buscema, R. Molenaar, V. Singh, L. Janssen, H. S. Van Der Zant, and G. A. Steele, Deterministic transfer of two-dimensional materials by all-dry viscoelastic stamping, *2D Mater.* **1**, 011002 (2014).
- [29] D. B. Williams and C. B. Carter, *Transmission Electron Microscopy* (Springer, New York, 2009).
- [30] T. Danz, T. Domröse, and C. Ropers, Ultrafast nanoimaging of the order parameter in a structural phase transition, *Science* **371**, 371 (2021).
- [31] See Supplemental Material at <http://link.aps.org/supplemental/10.1103/PhysRevLett.132.226201> for electromagnetic heating simulation details, bias-dependent dark field imaging, resistivity measurement of IBID Pt, correspondence of melting to time-dependent and total pulse energy, recovery dynamics of the charge density wave order, and acoustic resonance in diffraction peaks, which includes Refs. [18,32–40] and for a time-resolved TEM movie during 20 ns, 11.8 V pulses.
- [32] H. Ftouni, C. Blanc, D. Tainoff, A. D. Fefferman, M. Defoort, K. J. Lulla, J. Richard, E. Collin, and O. Bourgeois, Thermal conductivity of silicon nitride membranes is not sensitive to stress, *Phys. Rev. B* **92**, 125439 (2015).
- [33] A. Suzuki, M. Koizumi, and M. Doyama, Thermal evidences for successive CDW phase transitions in 1T-TaS₂, *Solid State Commun.* **53**, 201 (1985).
- [34] M. D. Núñez-Regueiro, J. M. Lopez-Castillo, and C. Ayache, Thermal conductivity of 1T-TaS₂ and 2H-TaSe₂, *Phys. Rev. Lett.* **55**, 1931 (1985).

- [35] S. Alaie, D.F. Goettler, Y.-B. Jiang, K. Abbas, M.G. Baboly, D.H. Anjum, S. Chaieb, and Z.C. Leseman, Thermal conductivity and nanocrystalline structure of platinum deposited by focused ion beam, *Nanotechnology* **26**, 085704 (2015).
- [36] A. Fernández-Pacheco, J.M. De Teresa, R. Córdoba, and M.R. Ibarra, Metal-insulator transition in Pt-C nanowires grown by focused-ion-beam-induced deposition, *Phys. Rev. B* **79**, 174204 (2009).
- [37] R. Langford, T.-X. Wang, and D. Ozkaya, Reducing the resistivity of electron and ion beam assisted deposited Pt, *Microelectron. Eng.* **84**, 784 (2007).
- [38] Y. Takahashi and E.F. Westrum Jr, Glassy carbon low-temperature thermodynamic properties, *J. Chem. Thermodyn.* **2**, 847 (1970).
- [39] D. Svetin, I. Vaskivskiy, S. Brazovskii, and D. Mihailovic, Three-dimensional resistivity and switching between correlated electronic states in 1T-TaS₂, *Sci. Rep.* **7**, 46048 (2017).
- [40] Y. Zhang, J. Li, W. Wang, H. Tian, W. Gao, J. Li, S. Sun, and H. Yang, Simulation of ultrafast electron diffraction intensity under coherent acoustic phonons, *Struct. Dyn.* **10** (2023).
- [41] T. E. Gage, D. B. Durham, H. Liu, S. Guha, I. Arslan, and C. Phatak, Nanosecond electron imaging of transient electric fields and material response, [arXiv:2306.01171](https://arxiv.org/abs/2306.01171).
- [42] E. J. Kirkland, *Advanced Computing in Electron Microscopy* (Springer US, New York, 2010).
- [43] D. Svetin, I. Vaskivskiy, P. Sutar, E. Goreshnik, J. Gospodaric, T. Mertelj, and D. Mihailovic, Transitions between photoinduced macroscopic quantum states in 1T-TaS₂ controlled by substrate strain, *Appl. Phys. Express* **7**, 103201 (2014).
- [44] T. Ritschel, J. Trinckauf, G. Garbarino, M. Hanfland, M. v. Zimmermann, H. Berger, B. Büchner, and J. Geck, Pressure dependence of the charge density wave in 1T-TaS₂ and its relation to superconductivity, *Phys. Rev. B* **87**, 125135 (2013).
- [45] K. Ziebeck, B. Dorner, W. Stirling, and R. Schollhorn, Kohn anomaly in the 1T₂ phase of TaS₂, *J. Phys. F* **7**, 1139 (1977).
- [46] Y. P. Varshni, Temperature dependence of the elastic constants, *Phys. Rev. B* **2**, 3952 (1970).
- [47] L.-Y. Gan, L.-H. Zhang, Q. Zhang, C.-S. Guo, U. Schwingenschlögl, and Y. Zhao, Strain tuning of the charge density wave in monolayer and bilayer 1T-TaS₂, *Phys. Chem. Chem. Phys.* **18**, 3080 (2016).
- [48] R. Venturini, A. Mraz, I. Vaskivskiy, Y. Vaskivskiy, D. Svetin, T. Mertelj, L. Pavlovič, J. Cheng, G. Chen, P. Amarasinghe, S. B. Qadri, S. B. Trivedi, R. Sobolewski, and D. Mihailovic, Ultraefficient resistance switching between charge ordered phases in 1T-TaS₂ with a single picosecond electrical pulse, *Appl. Phys. Lett.* **120**, 253510 (2022).